PHYSICAL REVIEW D **84,** 054006 (2011)

# Study of $\pi\pi$ correlations at LHC and RHIC energies in $pp$ collisions within the quark-gluon string model

M. S. Nilsson, L. V. Bravina, and E. E. Zabrodin*
*Department of Physics, University of Oslo, PB 1048 Blindern, N-0316 Oslo, Norway*

L. V. Malinina†
*Skobeltzyn Institute for Nuclear Physics, Moscow State University, RU-119899 Moscow, Russia*

J. Bleibel‡
*Institut für Physik, WA 331, Johannes Gutenberg Universität Mainz, D-55099 Mainz, Germany*
(Received 9 June 2011; published 12 September 2011)

The quark-gluon string model reproduces well the global characteristics of the $pp$ collisions at energies of $\sqrt{s} = 200$ GeV (RHIC) and $\sqrt{s} = 900$ GeV (LHC). In present paper the quark-gluon string model is employed for the description of femtoscopic characteristics of identical pions produced in the aforementioned reactions. The study is concentrated on the low multiplicity and multiplicity averaged events, where no collective effects are expected. The different procedures for fitting the one-dimensional correlation functions of pions are studied and compared with the space-time distributions extracted directly from the model. Particularly, it is shown that the double-Gaussian fit reveals the contributions coming separately from resonances and from directly produced particles. The comparison of model results with the experimental data favors a decrease in particle formation time with rising collision energy.

DOI: 10.1103/PhysRevD.84.054006 PACS numbers: 25.75.Gz, 13.85.−t, 24.10.Lx

## I. INTRODUCTION

Experiments at the Relativistic Heavy Ion Collider (RHIC) have demonstrated that hot and dense matter with partonic collectivity has been formed in ultrarelativistic Au + Au collisions at $\sqrt{s} = 200$ *A*GeV [1]. Proton-proton collisions are conventionally used as a reference to compare with nuclear collisions and to understand the observed collective effects. The new interest in general features of $pp$ collisions at ultrarelativistic energies appeared after the first publications of Large Hadron Collider (LHC) data obtained in $pp$ interactions at $\sqrt{s} = 900$ GeV and 7 TeV [2,3].

The Bose-Einstein enhancement in the production of two identical pions at low relative momenta was first observed in $\bar{p}p$ collisions about 50 years ago [4]. Since then, the developed correlation method, colloquially known at present as the ''femtoscopy technique,'' was successfully applied to the measurement of space-time characteristics of the production process at the distances of a few fermis (1 fm $= 10^{-15}$ m) (see, e.g., [5–7] and references therein). The space-time relative distances are ''measured'' by femtoscopy studies at the points where the particles stop to interact. This moment occurs at the very late stage of the collision, long after the quark-gluon plasma or any other exotic state of matter has disappeared. But signals like the geometric growth of the reaction zone and the specific features of the collective flow, generated by quark-gluon plasma pressure gradients, could be imprinted in the final state as very specific space-momentum correlations influencing particle spectra and femtoscopic radii.

The system created in ultrarelativistic $pp$ collisions at RHIC and especially at LHC energies can be similar to the system created in noncentral heavy-ion collisions because of the large energy deposited in the overlapping region and therefore can also demonstrate collective behavior. The strong argument supporting this point of view comes from the observation of the almost identical multiplicity and momentum dependencies of the femtoscopic radii in $pp$ and Au + Au collisions by the STAR collaboration at RHIC [8]. In particular, the transverse momentum dependence of the radii can be linked to the collective flow developed in the system [7]. The striking result obtained by the ALICE collaboration from study of the Bose-Einstein correlations in $pp$ collisions at $\sqrt{s} = 900$ GeV [9] is the absence of the transverse momentum dependence, whereas the increase of correlation radii with rising multiplicity is similar to that observed in relativistic heavy-ion collisions at energies up to RHIC.

The aim of the present article is to study hadronization processes in $pp$ collisions at ultrarelativistic energies using the momentum correlation technique within the Monte Carlo quark-gluon string model (QGSM) [10,11] and to compare results of calculations with the experimental data obtained at RHIC and LHC. This model describes

*Also at Skobeltzyn Institute for Nuclear Physics, Moscow State University, RU-119899 Moscow, Russia
†Also at Department of Physics, University of Oslo, PB 1048 Blindern, N-0316 Oslo, Norway
‡Also at Max-Planck-Institut für Intelligente Systeme, Heisenbergstr. 3, D-70569 Stuttgart, Germany

 

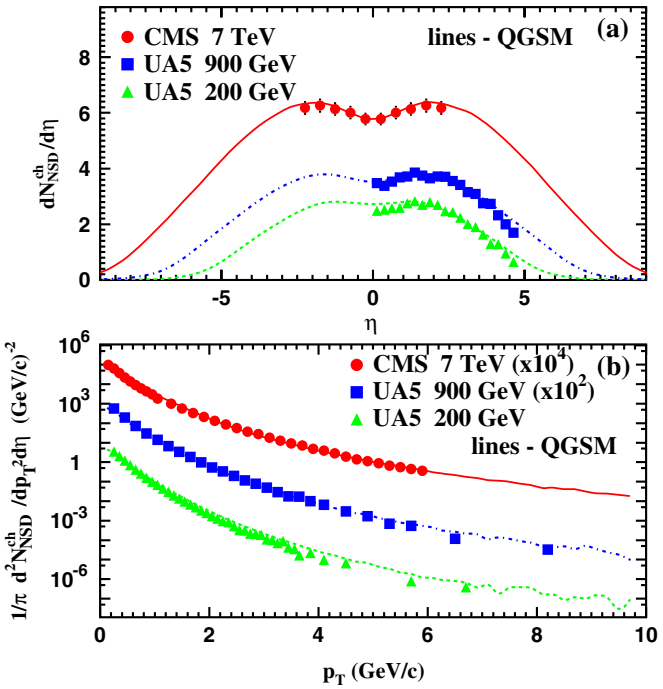


FIG. 1 (color online). (a) The charged particle pseudorapidity spectra and (b) their transverse momentum spectra in non-single-diffractive events calculated in QGSM for $pp$ collisions at $\sqrt{s} =$ 200 GeV (dashed lines), 900 GeV (dash-dotted lines) and 7 TeV (solid lines). Symbols denote the experimental data taken from [2,3,30].

successfully the main characteristics of $pp$ interactions, such as multiplicity, transverse momentum and (pseudo) rapidity distributions in a broad energy range from $\sqrt{s} =$ 200 GeV up to top LHC energy $\sqrt{s} = 7$ TeV [11]. We try to understand to what extent one is able to describe the correlation functions (CFs) in ultrarelativistic $pp$ collisions within the pure string model picture.

The paper is organized as follows. A brief description of the model features is presented in Sec. II. Special attention is given to the concept of the formation time, which plays a very important role for study of the femtoscopy correlations. Section III introduces the method of correlation functions employed by both the STAR and the ALICE collaboration. Model results obtained for $pp$ collisions at $\sqrt{s} = 200$ GeV and $\sqrt{s} = 900$ GeV are presented in Sec. IV. Comparison with the available experimental data is given as well. The proper choice of the baseline used in such measurements is discussed. The ability of the double-Gaussian fit to identify the contributions of string processes and resonances to the correlation functions is demonstrated. Finally, conclusions are drawn in Sec. V.

## II. THE MODEL

### A. Basic features

Our model is the Monte Carlo realization of the quark-gluon string model developed in [12]. Similarly to the dual parton model [13], QGSM is based on Gribov's Reggeon field theory (GRT) [14] accomplished by a string phenomenology of particle production in inelastic hadron-hadron collisions. The model incorporates the Field-Feynman algorithm [15] of string fragmentation. It enables one to consider emission of hadrons from both ends of the string with equal probabilities. As independent degrees of freedom QGSM includes octet and decuplet baryons, octet and nonet vector and pseudoscalar mesons, and their antiparticles. Pauli blocking is taken into account by excluding the already occupied final states from the available phase space.

Strings in the QGSM can be produced as a result of the color exchange mechanism or, like in diffractive scattering, due to momentum transfer. The Pomeron, which is a pole with an intercept $\alpha_P(0) > 1$ in the GRT, corresponds to the cylinder-type diagrams. The $s$-channel discontinuities of the diagrams, representing the exchange by $n$ Pomerons, are related to the process of $2k(k \leq n)$ string production. If the contributions of all $n$-Pomeron exchanges to the forward elastic scattering amplitude are known, the Abramovskii-Gribov-Kancheli cutting rules [16] enable one to determine the cross sections for $2k$ strings. The hard gluon-gluon scattering and semihard processes with quark and gluon interactions are also incorporated in the model via the so-called hard Pomeron exchange [11,17], first discussed in [18]. The hard Pomeron is nowadays a standard feature attributed to a variety of GRT-based microscopic models, such as the dual parton model [13,19], PHOJET [20], QGSJET [21] and EPOS [22]. Its presence seems to be necessary to describe the rise of multiplicity at midrapidity and $p_T$ spectra of secondaries in $pp$ interactions at LHC energies within the QGSM [11]. Further details of the Monte Carlo version of QGSM and its extension to $A + A$ collisions can be found in [10,11,23].

Figure 1 displays the pseudorapidity and transverse momentum distributions of charged particles produced in nonsingle diffractive $pp$ collisions at $\sqrt{s} = 200$ GeV, 900 GeV and 7 TeV, respectively. Experimental data are also plotted. Since the model reproduces the bulk characteristics of the collisions quite well, we are encouraged to apply the QGSM for the analysis of particle interferometry. Note, however, that the GRT does not provide the space-time picture of the system evolution, thus leaving room for the assumptions concerning the femtoscopy correlations quite open. Here one has to rely on approaches developed within the framework of the string phenomenology.

### B. QGSM and particle coordinates

The space-time evolution of the collisions starts from the interacting partons, i.e., quarks, diquarks and sea quarks distributed randomly in the projectile-target overlapping region. The strings between them are stretching and subsequently decaying into hadrons. Because of the uncertainty principle it takes time to create a hadron from constituent

quarks. Also, hadrons are composite particles, and this circumstance makes the definition of the formation time model dependent. In the framework of the Lund string model [24] two definitions of the formation time or, equivalently, formation length are eligible [25]. In the "yo-yo" case it corresponds to the time/coordinate of the first intersection point of the hadron constituents ("yo-yo" formation time). In the so-called constituent case it corresponds to the time/coordinate of the point of rupture of the string (constituent formation time). In the present version of the QGSM the constituent formation time is used. The string length $L = M_s/2\kappa$ depends on its mass $M_s$ and on the string tension $\kappa$. The mass of the string is not fixed. It is determined by the generation of longitudinal and transverse momenta of valence quarks at the string ends, that depend on the momenta of colliding hadrons. The length of the string varies from the maximum value determined by the momentum of the incident hadron to the minimum value determined by the pion mass. Therefore, for the formation of a resonance the mass and length of the string must be much larger than for production of a pion.

The formation time $t_i^*$ and coordinate $z_i^*$ of $i$th hadron in the string center of mass can be expressed via its energy $E_i^*$, its longitudinal momentum $p_{zi}^*$ and the longitudinal momenta/energies of all hadrons produced by the decay of this string (see *Appendix*)

$$t_i^* = \frac{1}{2\kappa}\left(M_s - 2\sum_{j=1}^{i} p_{zj}^*\right), \quad (1)$$

$$z_i^* = \frac{1}{2\kappa}\left(M_s - 2\sum_{j=1}^{i} E_j^*\right). \quad (2)$$

Then we calculate $t_i$ in the laboratory frame and make the propagation of the coordinates to this point $(x_i, y_i, z_i, t_i)$: $a_i = a_{0i} + t_i p_{ai}/E_i$, $a = x, y, z$. The initial spatial distribution of partons in a proton is found to be insignificant for the pion coordinate distributions at freeze-out, which are dominated by both the formation time of hadrons and decay lengths of resonances. To study the possible reduction of the formation time because of, e.g., increase of the string tension with rising incident energy we introduce in Eqs. (1) and (2) the scaling parameter $\alpha$, i.e., $\kappa = \alpha\kappa_0$, where $\kappa_0 = 0.88$ GeV/fm is the default value of the string tension coefficient in the QGSM found from comparison with experimental data at lower energies [10]. The coordinate distributions of pions at freeze-out are shown in Fig. 2 for $pp$ collisions at $\sqrt{s} = 900$ GeV with $\alpha = 1$, 1.5 and 3. One can see that increase of $\alpha$ makes the coordinate distributions narrower.

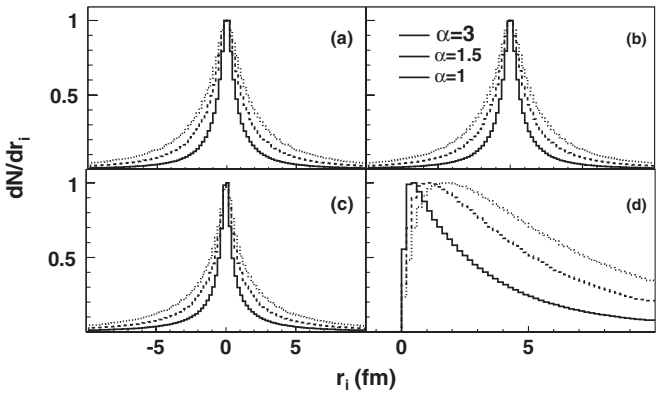


FIG. 2. The $dN/dr_i$, $r_i = x$ (a), $y$ (b), $z$ (c), $t$ (d) distributions of pions at freeze-out in $pp$ collisions at $\sqrt{s} = 900$ GeV with $\alpha = 1$ (dotted line), $\alpha = 1.5$ (dashed line) and $\alpha = 3$ (solid line).

## III. THE CORRELATION FUNCTION REPRESENTATIONS

The momentum correlations are usually studied with the help of correlation functions of two or more particles. Particularly, the two-particle correlation function $\mathrm{CF}(p_1, p_2) = A(p_1, p_2)/B(p_1, p_2)$ is defined as a ratio of the two-particle distribution from the same event $A(p_1, p_2)$ to the reference one. In experimental analysis the reference distribution is typically constructed by mixing the particles from different events of a given class.

In our simulations the weight of each particle pair is calculated according to quantum statistics, using particle four-momenta $p_i$ and four-coordinates $x_i$ of the emission points: $w = 1 + \cos(q \cdot \Delta x)$, where $q = p_1 - p_2$ and $\Delta x = x_1 - x_2$. Note that the weight $w$ used here has equally enhanced and reduced values. In this way quantities like the average multiplicity are not systematically affected by the weighting. The CF is here defined as a ratio of the weighted histogram of the pair kinematic variables to the unweighted one. This "ideal" case, $\mathrm{CF}_{\mathrm{ideal}}(p_1, p_2) = A(p_1, p_2, w)/A(p_1, p_2)$, uses unweighted pairs from the same events as the reference.

In experiments one utilizes unweighted mixed pairs from different events as the reference, namely $\mathrm{CF}_{\mathrm{realistic}}(p_1, p_2) = A(p_1, p_2, w)/B(p_1, p_2)$. Among other effects there is a difference between the ideal pair distribution $A(p_1, p_2)$ and the mixed one $B(p_1, p_2)$ due to the presence of energy-momentum conservation for the pairs from the same event and absence of it in pairs from the mixed ones. This causes a smooth increase of $\mathrm{CF}_{\mathrm{realistic}}$ with $q$, which reflects the fact that due to energy-momentum conservation the probability of two-particle emittence in the same direction is smaller than that in opposite directions. Therefore, a more complex fitting procedure is needed for the "realistic CF" than for the "ideal CF."

Generally, the correlations are measured as a function of pair relative momentum four vector $q$. An invariant form of this momentum difference commonly used in the one-dimensional correlation analysis is $q_{\mathrm{inv}} = \sqrt{q_0^2 - |q|^2}$. In both the STAR [8] and the ALICE [9] experiments the correlation function is fitted to a single-Gaussian

$$\mathrm{CF}_{\mathrm{single}}(q_{\mathrm{inv}}) = [1 + \lambda \exp(-R_{\mathrm{inv}}^2 q_{\mathrm{inv}}^2)] D(q_{\mathrm{inv}}), \quad (3)$$

where the function $D(q_{\rm inv})$ takes into account any non-femtoscopic correlations including the long-range correlations due to energy-momentum conservation described above. The parameters $R_{\rm inv}$ and $\lambda$ describe the size of pion sources and the correlation strength, respectively. Here $R_{\rm inv}$ is defined in the pair rest frame (PRF). Concerning the fit given by Eq. (3) we have to note that the best way to compare the model simulations with the experimental data is the direct comparison of the correlation functions. Unfortunately, the CFs are not always available and one has to compare the results of the fit, that is more complicated. For instance, choice of the baseline $D(q_{\rm inv})$ is rather arbitrary. The baseline should describe the CF behavior at large $q_{\rm inv}$ where only the *conservation laws* work, but the region of small $q_{\rm inv}$ remains *terra incognita*. Different experiments employ different extrapolations of the baseline to small $q_{\rm inv}$, e.g., polynomial extrapolations, EMCIS-FIT [8], Monte Carlo simulations with PYTHIA and PHOJET [9], that give some specific behavior at small $q_{\rm inv}$ due to strong jet contribution in these models, especially noticeable at large $k_t$. In order to reproduce the experimental fitting procedures in a model independent way and make a consistent comparison of our simulations with different experiments we will use below a flat baseline with $D(q_{\rm inv}) = 1$ for STAR and ALICE data.

The correlation strength parameter $\lambda$ can differ from unity due to the contribution of long-lived resonances, particle misidentification and coherence effects. The 1D correlation functions were studied within the different ranges of the average pair transverse momentum $k_T = |\vec{p}_{t,1} + \vec{p}_{t,2}|/2$ in the midrapidity region.

If large statistics sets are available it is possible to perform the 3D correlation analysis. Within realistic models, the directional and velocity dependence of the correlation function can be used to get information about both the duration of the emission and the form of the emission region, as well as to reveal the details of the production dynamics [5–7]. For these purposes the correlation functions can be analyzed in terms of the out, side and logitudinal components of the relative momentum vector $\mathbf{q} = \{q_{\rm out}, q_{\rm side}, q_{\rm long}\}$ [26,27]. Here $q_{\rm out}$ and $q_{\rm side}$ denote the transverse components of the vector $\mathbf{q}$, and the direction of $q_{\rm out}$ is parallel to the transverse component of the pair three-momentum. The corresponding correlation widths are usually parametrized in terms of the Gaussian correlation radii $R_i$

$$\mathrm{CF}(p_1, p_2) = 1 + \lambda \exp(-R_{\rm out}^2 q_{\rm out}^2 - R_{\rm side}^2 q_{\rm side}^2 - R_{\rm long}^2 q_{\rm long}^2). \tag{4}$$

The three-dimensional analysis is performed in the longitudinal comoving system (LCMS), where the pair momentum along the beam vanishes. It is possible to compare the radii measured in LCMS with $R_{\rm inv}$ by making a boost of all radii from LCMS to PRF, namely, $R_{\rm out\,PRF} = \gamma_T R_{\rm out}$, $R_{\rm side\,PRF} = R_{\rm side}$, $R_{\rm long\,PRF} = R_{\rm long}$ and averaging these radii.

The method used by STAR and ALICE experiments is to create a 3D correlation function by filling a three-dimensional histogram with the full $\mathbf{q} = \{q_{\rm out}, q_{\rm side}, q_{\rm long}\}$ vector in different ranges of the average pair transverse momentum $k_T = |\vec{p}_{t,1} + \vec{p}_{t,2}|/2$.

## IV. RESULTS AND DISCUSSION

The two-pion correlation functions $\mathrm{CF}(q_{\rm inv})$ simulated for $pp$ collisions within the QGSM model with the scaling parameters $\alpha = 1, 2$ and 3 are shown in different $k_T$ ranges in Fig. 3 and 4 for $\sqrt{s} = 200$ GeV and $\sqrt{s} = 900$ GeV, respectively. The denominator of the CF was calculated by means of the mixing procedure described in Sec. III. As expected, smaller formation times lead to smaller freeze-out radii of the particle sources and, therefore, to

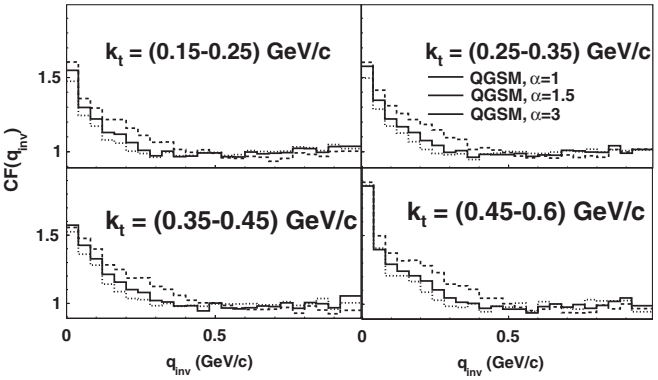


FIG. 3. The $\pi^+\pi^+$ CFs for $pp$ at $\sqrt{s} = 200$ GeV in four $k_T$ bins obtained by mixed pair reference distribution. Cuts are $|\eta| < 0.5$ and $0.12\ \mathrm{GeV}/c \leq p_T \leq 0.8\ \mathrm{GeV}/c$, as in the STAR experiment. Calculations are performed with $\alpha = 1$ (dotted line), $\alpha = 1.5$ (solid line) and $\alpha = 3$ (dashed line).

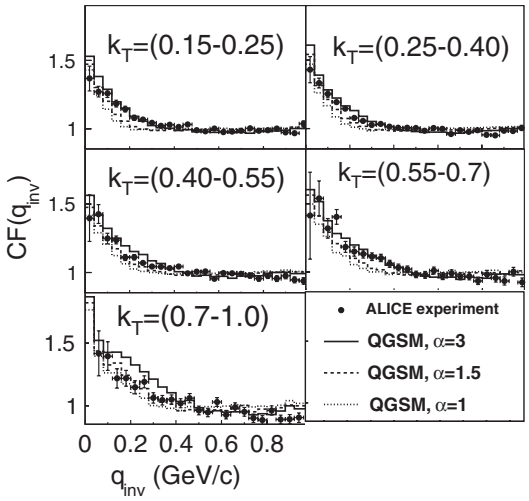


FIG. 4. The same as Fig. 3 but for $\sqrt{s} = 900\ \mathrm{GeV}/c$. Cuts are $|\eta| < 0.8$ and $0.15\ \mathrm{GeV}/c \leq p_T \leq 1.0\ \mathrm{GeV}/c$. Calculations with $\alpha = 1$ (dotted line), $\alpha = 1.5$ (dashed line) and $\alpha = 3$ (solid line) are compared to ALICE results [9] with multiplicity $M \leq 6$.

larger CFs in the interval $0 \leq q_{\rm inv} \leq 0.5$ GeV/$c$. In Fig. 4 the correlation functions obtained with the QGSM are directly compared to those measured by the ALICE collaboration. The ALICE analysis performed for the minimum bias event sample gives for the value of the average pseudorapidity density $\langle dN_{\rm ch}/d\eta \rangle = 3.6$, that coincides with the results of the QGSM simulations. We compare the QGSM low multiplicity sample with the ALICE data at low multiplicity bin $M \leq 6$. The best description is achieved for the scaling parameter equal to 3. In Fig. 4 one can see that the agreement between the shapes of the correlation functions calculated within the QGSM and measured by the ALICE is rather good till $k_T < 0.7$ GeV/$c$. In the last $k_T$ bin $0.7 \leq k_T \leq 1.0$ GeV/$c$ the experimental correlation function is about 15% narrower than the QGSM one. To understand this effect better the realistic correlation functions without quantum statistics weights, i.e."baselines", were constructed in different $k_T$ bins as displayed in Fig. 5. The energy-momentum conservation produces the long-range correlation effects at large $q_{\rm inv}$, for which the calculated values of the CFs lie above the unity. In Ref. [9] a good description of the long-range correlations was obtained within the PYTHIA and PHOJET models. In Fig. 5 the QGSM baseline $D(q_{\rm inv})$ demonstrates complicated behavior qualitatively similar to that of the PYTHIA/PHOJET baselines but a bit flatter in low $q_{\rm inv}$ interval for large $k_T$ bins.

Figure 6 presents the $k_T$ dependence of $R_{\rm inv}$ obtained from the fit to Eq. (3) with the flat baseline of the QGSM CFs, shown in Figs. 3 and 4. The available STAR and ALICE data points with flat baselines [8,9] are averaged over the multiplicity and compared with the multiplicity averaged QGSM correlation functions. The best agreement with the STAR data [8] was obtained for calculations with $\alpha = 1.5$.

It was reported in [9] that if PHOJET/PYTHIA baselines are chosen the correlation radii are practically independent on $k_T$ within the studied transverse momentum range, however, the strength of the $k_T$ dependence relies heavily on the baseline hypothesis. The ALICE conclusion about the absence of $k_T$ dependence is based on the assumption that both PHOJET and PYTHIA correctly describe the nonfemtoscopic effects at low $q_{\rm inv}$ possibly related to minijets. In this case the enhancement at low $q_{\rm inv}$ in the large $k_T$ bins is misinterpreted as Bose-Einstein enhancement. We see, however, that by assigning Bose-Einstein weights to all pion pairs we are able to reproduce the enhancement at low-$q_{\rm inv}$ shown in Fig. 4. In such a case it will be improper to use the PHOJET/PYTHIA or our own QGSM baseline to exclude the assumed nonfemtoscopy correlations at low $q_{\rm inv}$. The rather successful description of the ALICE points within such an approach suggests that there is no room for nonfemtoscopic correlations at low $q_{\rm inv}$ up to $k_T < 0.7$ GeV/$c$.

The ALICE and STAR data points obtained with the flat baseline reveal a similar slope in Fig. 6, which is described rather well by the QGSM calculations with the scaling factors $\alpha = 1.5$ and $\alpha = 3$, respectively. However, the higher $k_T$ bins have larger deviations from the experimental points.

It is helpful to understand the origin of the strong $k_T$ dependence of the correlation radii in the QGSM model. The Lund hadronization schema described by Eqs. (1) and (2) introduces automatically the space-momentum correlations. The "$p$-$x$" correlations for the direct pions displayed in Fig. 7 look similar to the space-momentum correlations in hydrodynamic models, where they arise

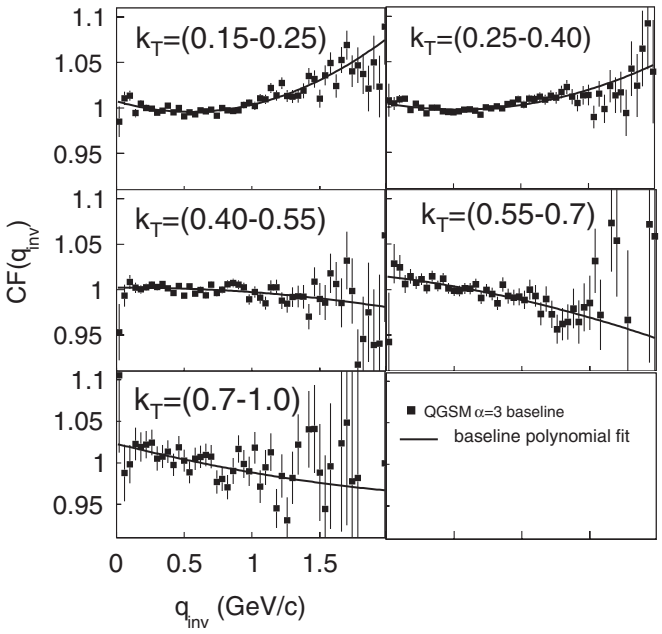


FIG. 5. The baseline for $\pi^+\pi^+$ correlation functions extracted from QGSM calculations (full circles) of $pp$ collisions at $\sqrt{s} = 900$ GeV in different $k_T$ intervals. Solid lines denote the fit to polynomial $D(q_{\rm inv}) = a + bq_{\rm inv} + cq_{\rm inv}^2$.

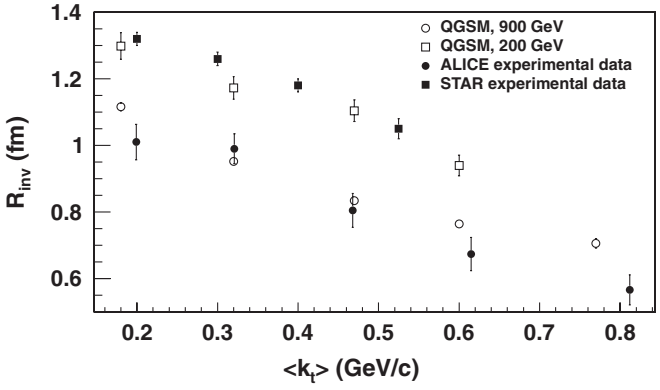


FIG. 6. One-dimensional $\pi^+\pi^+$ correlation radii as functions of $k_T$ in $pp$ collisions at $\sqrt{s} = 200$ GeV (squares) and $\sqrt{s} = 900$ GeV (circles). Open symbols denote STAR [8] and ALICE [9] experimental data, full symbols present QGSM calculations with $\alpha = 1.5$ (200 GeV) and $\alpha = 3.0$ (900 GeV), respectively. Both the model results and the data are obtained from the fit to Eq. (3) with the flat baseline.

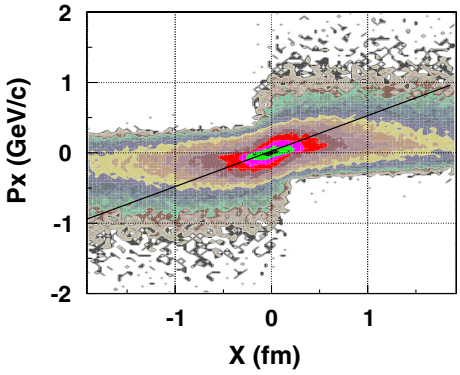


FIG. 7 (color online). The space-momentum correlations of direct pions produced in QGSM calculated $pp$ collisions at $\sqrt{s} = 900$ GeV. Line is drawn to guide the eye.

due to transverse collective flow. Note that only the particles with nearby velocities in their center-of-mass system contribute to the correlation function. If the "$p$-$x$" correlations are absent, the whole source is "seen" by the CF in any chosen $k_T$ range. Thus, there should be no $k_T$ dependence of the correlation radii. In the presence of the "$p$-$x$" correlations the particles with close momenta come from nearby space regions of the source. Therefore, one is measuring not the real geometrical size of the source, but rather the size of the regions which emit particles of a given momenta, the so-called regions of homogeneity [28]. Higher $k_T$ pairs should have narrower coordinate distributions due to larger "focusing effect". It originates from the fact that particles with large momenta fly away from each other much quicker than particles with small momenta, so in order to be correlated they have to be very close in the coordinate space. In Fig. 8(a) and 8(b) the transverse coordinate distributions are shown in the pair rest frame together with the corresponding correlation functions $\mathrm{CF_{ideal}}$ for the direct pions in three $k_T$ ranges, namely KT1 = (0.1–0.25) GeV/$c$; KT3 = (0.4–0.55) GeV/$c$ and KT5 = (0.7–1.0) GeV/$c$. We see that the widths of the $X_{\mathrm{PRF}}$ distributions decrease with rising $k_T$ and the corresponding $\mathrm{CF_{ideal}}$ become narrower. These widths are reproduced within error bars by the fit of $\mathrm{CF_{ideal}}$ to the Gaussian given by Eq. (3) with $D(q_{\mathrm{inv}}) = 1$.

The important factor influencing the coordinate distributions is the ratio of direct pions to pions from resonance decay. Table I presents the fractions of pions from decay of the resonances most essentially contributed to the correlation functions. The path length $l^* \simeq p_d/m_\pi\Gamma$ of these states in the c.m. frame of two identical pions at small value of $q_{\mathrm{inv}}$ is listed in Table I also. Here $p_d$ is the momentum of the decay pion in the resonance rest frame [29], $m_\pi$ is the pion mass and $\Gamma$ is the decay width. The pions from the decays of rather long-lived resonances $\omega$ and $K^*$ cause appearance of the exponential tails in the pion emission function, which distorts the Gaussian-like shape of the CF,

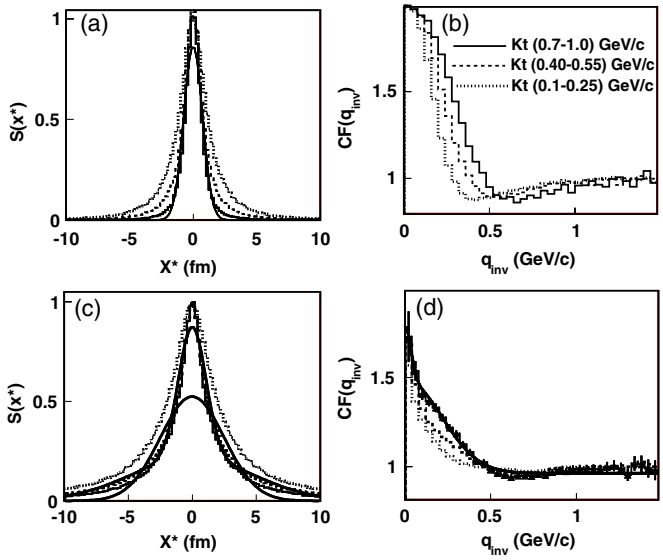


FIG. 8 (color online). (a) Coordinate distributions of the direct pions in PRF in QGSM calculated $pp$ collisions at $\sqrt{s} = 900$ GeV with $\alpha = 3$. The three transverse momentum intervals are KT1 = (0.1–0.25) GeV/$c$ (dotted histogram), KT3 = (0.4–0.55) GeV/$c$ (dashed histogram) and KT5 = (0.7–1.0) GeV/$c$ (solid histogram). The single-Gaussian fit for the KT5 bin is shown by the solid line. (b) $\mathrm{CF_{ideal}}$ for KT1 (dotted histogram), KT2 (dashed histogram) and KT3 (solid histogram). (c) The same as (a) but for all pions, the single and the double-Gaussian fits are shown for KT5 bin by the solid lines. (d) The same as (b) but for all pions, the double-Gaussian fit is shown for KT5 bin by the solid line.

see Fig. 8(c) and 8(d). Their relative contribution decreases with increasing $k_T$ due to kinematical reasons, whereas the relative contributions of direct pions and pions from $\rho$ decays increase as displayed in Fig. 9. This effect also leads to decrease of the correlation radii with increasing $k_T$. The essentially non-Gaussian coordinate distributions that include contributions from resonances cannot be fitted well to a single Gaussian, however, the double-Gaussian fit reproduces its shape properly, see Fig. 8(c). By fitting the corresponding CFs to a single Gaussian one cannot describe the narrow peak produced by pions from the resonance decays at low $q_{\mathrm{inv}}$. On the other hand, using the double-Gaussian fitting procedure similar to the one suggested in [29]

TABLE I. The fraction of pions from decay of main resonance species in QGSM and the path length $l^*$ of these states.

| | $l^*$ (fm) | 200 GeV | 900 GeV |
|---|---|---|---|
| Direct $\pi^+$ | ⋯ | 46.9% | 37.5% |
| $\pi^+$ from $\rho^{0,+} \to \pi^{-,0}\pi^+$ | 3.3 | 37.1% | 40.7% |
| $\pi^+$ from $\omega \to \pi^0\pi^-\pi^+$ | 28.1 | 11.2% | 15.9% |
| $\pi^+$ from $K^{*,+}(\bar{K}^{*,0}) \to K\pi^+$ | 8.0 | 4.2% | 5.5% |

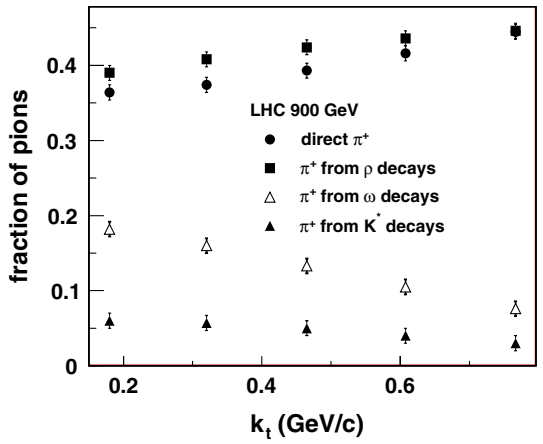


FIG. 9 (color online). The fractions of pions coming from resonance decays and direct ones as functions of the average pair momentum $k_T$ in QGSM calculated $pp$ collisions at $\sqrt{s} = 900$ GeV. The symbols denote directly produced pions (full circles) and pions coming from the decays of $\rho$ mesons (full squares), $\omega$ mesons (open triangles) and $K^*$ (full triangles), respectively.

$$\mathrm{CF}_{\mathrm{double}}(q_{\mathrm{inv}}) = [1 + \lambda_1 \exp(-R^2_{\mathrm{inv},1} q^2_{\mathrm{inv}}) + \lambda_2 \exp(-R^2_{\mathrm{inv},2} q^2_{\mathrm{inv}})] D(q_{\mathrm{inv}}), \quad (5)$$

where parameters $R_{\mathrm{inv}(1,2)}$ and $\lambda_{(1,2)}$ describe the sizes and the correlation strengths of the direct pion source and the one of the pions from the resonance decays, respectively, one gets a much better description of the CF shape at low $q_{\mathrm{inv}}$, as shown in Fig. 8(d).

In order to understand to what extent one is able to describe the correlation functions of all particles including the resonances by the different fitting procedures we make a comparison of the extracted values of $R_{\mathrm{inv}}$ with the

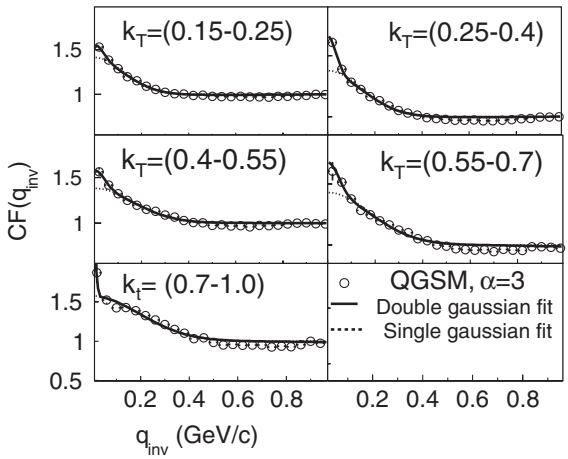


FIG. 10. The fit of pion correlation functions, obtained in QGSM calculated $pp$ collisions at $\sqrt{s} = 900$ GeV with $\alpha = 3$, to single Gaussian (dotted line) and double Gaussian (solid line) in five $k_T$ bins.

TABLE II. Gaussian widths $\sigma X^{\mathrm{all}}_{\mathrm{PRF}}$ of the coordinate distributions in PRF shown in Fig. 8(c) for single and double-Gaussian fit in three transverse momentum intervals $0.1 \le k_T \le 0.25$ GeV/$c$ (KT1), $0.4 \le k_T \le 0.55$ GeV/$c$ (KT3) and $0.7 \le k_T \le 1.0$ GeV/$c$ (KT5), respectively.

| | $\sigma X^{\mathrm{all}}_{\mathrm{PRF}}$ (fm) | | |
|---|---|---|---|
| Method | KT1 | KT3 | KT5 |
| single-Gaussian | 3.37 | 2.45 | 2.96 |
| double-Gaussian | 1.48 | 1.08 | 1.00 |
| | 5.35 | 4.72 | 4.23 |

Gaussian widths of the coordinate distributions in the pair rest frame. The comparison is presented in Fig. 8(c) for the ideal correlation functions $\mathrm{CF}_{\mathrm{ideal}}$ and in Fig. 10 for the realistic CFs. The extracted parameters are listed in Table II and III, respectively, for three $k_T$ ranges, namely, KT1 = (0.1–0.25) GeV/$c$; KT3 = (0.4–0.55) GeV/$c$ and KT5 = (0.7–1.0) GeV/$c$. Because of the sharp peak of the correlation functions at low $q_{\mathrm{inv}}$ the two radii restored by the double-Gaussian fit vary considerably. The first one is of the order of 1 fm and has a tendency to decrease with rising $k_T$, whereas the second one is always larger than 3 fm and increases to 13–14 fm at high transverse momenta. The second Gaussian is quite narrow thus leading to a hair-width difference between the single-Gaussian and double-Gaussian curves at $q_{\mathrm{inv}} > 0.1$ GeV/$c$.

The ideal 3D correlation functions for $\sqrt{s} = 200$ GeV and $\sqrt{s} = 900$ GeV, constructed for the minimum bias events and low multiplicity bin, are displayed in Fig. 11 and 12, respectively. The calculations were done with $\alpha = 1.5$ and $\alpha = 3.0$, and the full 3D fit to the 3D Gaussian given by Eq. (4) was performed. The extracted $R_i$ as

TABLE III. Parameters $R_{\mathrm{inv}}$ extracted from Fig. 8(c) and 10 by using different fitting strategies: *1*—ideal CF is fitted to the single-Gaussian Eq. (3) with $D(q_{\mathrm{inv}}) = 1$; *2*—"realistic" CF is fitted to the single-Gaussian Eq. (3) with $D(q_{\mathrm{inv}}) = 1$; *3*—realistic CF is fitted to the single-Gaussian Eq. (3) with $D(q_{\mathrm{inv}}) = a + bq_{\mathrm{inv}} + cq^2_{\mathrm{inv}}$; *4*—realistic CF is fitted to the double-Gaussian Eq. (5) with $D(q_{\mathrm{inv}}) = 1$; *5*—realistic CF is fitted to the double-Gaussian Eq. (5) with $D(q_{\mathrm{inv}}) = a + bq_{\mathrm{inv}} + cq^2_{\mathrm{inv}}$. The selected transverse momentum intervals are the same as in Table II.

| | $R_{\mathrm{inv}1(2)}$ (fm) | | |
|---|---|---|---|
| Method | KT1 | KT3 | KT5 |
| 1 | 1.00 | 0.77 | 0.66 |
| 2 | 1.26 | 0.84 | 0.71 |
| 3 | 1.10 | 0.84 | 0.71 |
| 4 | 1.23 | 0.81 | 0.71 |
| | 5.04 | 3.26 | 13.97 |
| 5 | 1.05 | 0.81 | 0.71 |
| | 3.61 | 3.25 | 13.83 |

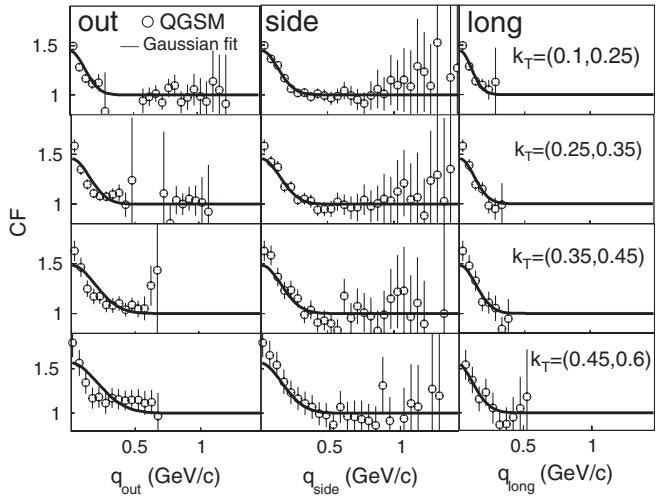


FIG. 11. Projections of the 3D Cartesian representations of the correlation functions onto the $q_{\rm out}$, $q_{\rm side}$, and $q_{\rm long}$ axes, for the minimum bias events from $pp$ collisions at 200 GeV for four $k_T$ ranges. To project onto one $q$ component, the others are integrated over the range $0 \le q_i \le 0.12$ GeV$/c$.

functions of average $k_T$ are presented in Fig. 13 and 14. One can see that the experimental points are rather close to the QGSM ones especially for ALICE experimental data, see Fig. 14, where the low multiplicity bin is considered. Note that no integration over multiplicity was done in both cases. At 200 GeV all radii demonstrate the weak decrease with $k_T$, whereas at 900 GeV the radii $R_{\rm out}$ and $R_{\rm side}$ are rather flat, the first point in $R_{\rm out}$ is lower than the other ones, and only $R_{\rm long}$ demonstrates the decrease with rising $k_T$ as was observed by the ALICE collaboration at low multiplicity.

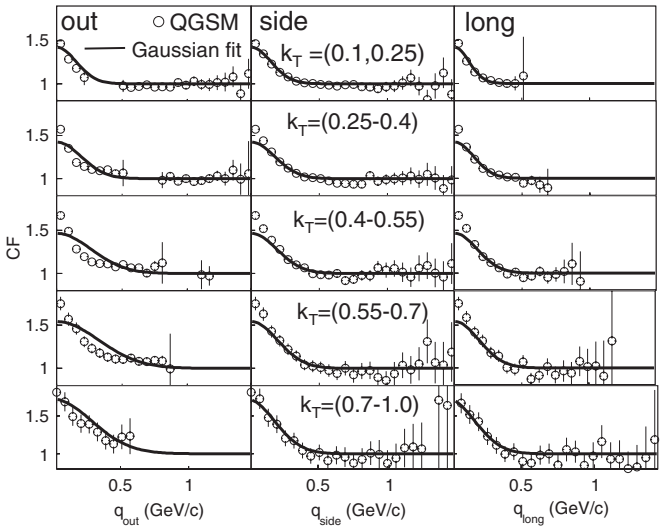


FIG. 12. The same as Fig. 11 but for the low multiplicity bin $N_{\rm ch} < 11$ of $pp$ collisions at 900 GeV in five $k_T$ ranges.

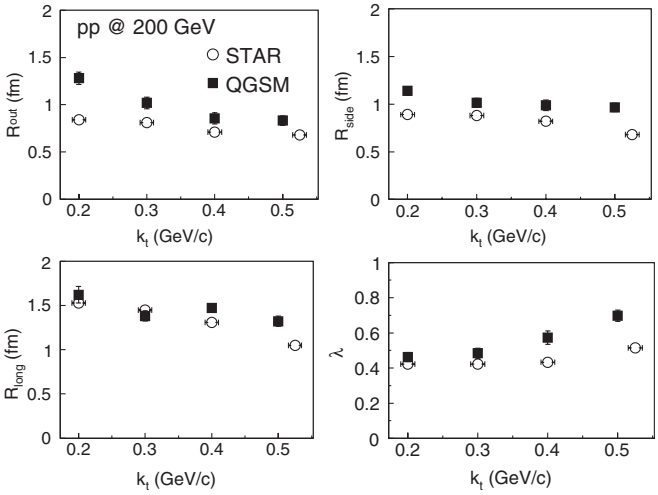


FIG. 13. Three-dimensional $\pi^+\pi^+$ correlation radii as functions of $k_T$ in $pp$ collisions at $\sqrt{s} = 200$ GeV for minimum bias events. Open circles denote STAR experimental data, full squares present QGSM calculations with $\alpha = 1.5$. Both the model results and the data are obtained from the fit to Eq. (4).

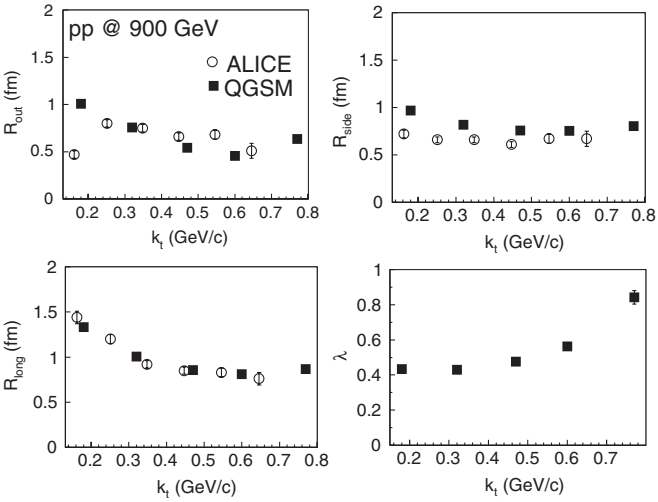


FIG. 14. The same as Fig. 13 but for the low multiplicity bin $N_{\rm ch} < 11$ of $pp$ collisions at $\sqrt{s} = 900$ GeV. QGSM calculations are with $\alpha = 3$.

## V. CONCLUSIONS

The following conclusions can be drawn from our study. QGSM calculations show strong dependence of the correlation radius on the transverse momentum of a pion pair. Similar dependence has been observed by the STAR Collaboration, while the ALICE Collaboration reported almost constant $R_{\rm inv}$ with increasing $k_T$. However, if the flat baseline is employed instead of the one simulated by PYTHIA and PHOJET, the ALICE data demonstrate the noticeable $k_T$ dependence as well. The origin of such a dependence in the QGSM is traced to the space-momentum correlations attributed to microscopic string models. If these correlations

would be absent, the correlation radius $R_{\rm inv}$ would be independent on the pair transverse momentum.

Pions in the model are produced either directly in the processes of string fragmentation or from the decays of resonances. The relative contribution of the long-lived resonances to pion emission function decreases with rising $k_T$, while the corresponding contributions of direct processes and short-lived resonances increase. Therefore, the correlation radii of pions also decrease with an increase in the pair transverse momentum. The fit of the 1D correlation functions to the double Gaussian provides a good description of the shape of the CFs at low $q_{\rm inv}$ range and enables us to separate the contributions from the direct pions and pions from the resonances.

It was expected that the size of the freeze-out region in $pp$ collisions should increase with rising c.m. energy from $\sqrt{s} = 200$ GeV to $\sqrt{s} = 900$ GeV due to the increase of interaction cross section and the number of produced resonances. Surprisingly, the radii measured by femtoscopy at $\sqrt{s} = 200$ GeV are the same or even smaller than the ones at $\sqrt{s} = 900$ GeV, as seen in Fig. 6. The radii obtained within the standard Lund scenario of string breaking and the constituent formation time, implemented in the QGSM, appear to be larger compared to the experimental data. Our analysis favors reduction of the formation time with increasing energy of hadronic collision. One of the possible solutions is the process of string-string interaction via, e.g., fusion of strings that leads to an increase of the string tension.

## ACKNOWLEDGMENTS

Fruitful discussions with A. Kisiel, R. Kolevatov, K. Mikhailov and Yu. Sinyukov are gratefully acknowledged. This work was supported by the Norwegian Research Council (NFR) under Contract No. 185664/V30.

## APPENDIX: SPACE-TIME COORDINATES OF PRODUCED HADRONS

Following Refs. [24,25] let us consider 1 + 1 fragmentation model of $q\bar{q}$ string of mass $M_s$ with massless constituents at the ends, as displayed in Fig. 15. The Hamiltonian of such a system is

$$H = |p_1| + |p_2| + \kappa|z_1 - z_2|, \tag{A1}$$

where $|p_1|$ and $|p_2|$ are the momenta of the quark and antiquark, $z_1$ and $z_2$ are their coordinates, and $\kappa$ is the string tension. The equation of motion for the constituents reads

$$\frac{dp}{dt} = \pm\kappa, \tag{A2}$$

with the sign depending on the direction of motion of the constituent. At a certain time $t_i$ the string breaks via formation of $q_i\bar{q}_i$ pair. The final hadrons are produced as a result of $\bar{q}_{i-1}q_i$ coalescence. Their energy and momentum are

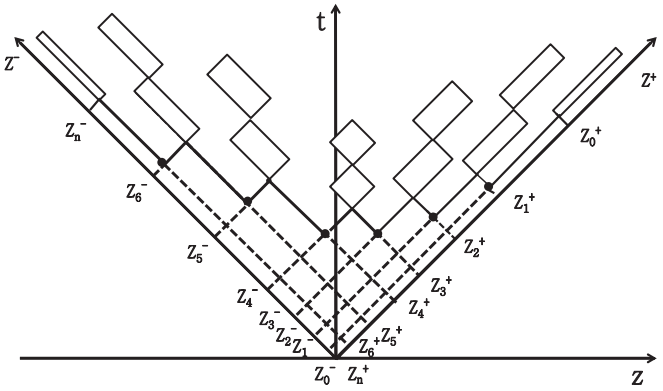


FIG. 15. Space-time evolution of the 1 + 1 dimensional Lund string. See text for details.

$$E_i = \kappa(z_{i-1} - z_i), \tag{A3}$$

$$p_i = \kappa(t_{i-1} - t_i), \tag{A4}$$

respectively. In terms of the light cone variables $p^\pm = E \pm p$, $z^\pm = t \pm z$ one gets for the $i$th hadron within the ''constituent'' picture of hadron formation

$$p_i^+ = \kappa(z_{i-1}^+ - z_i^+), \tag{A5}$$

$$p_i^- = \kappa(z_i^- - z_{i-1}^-). \tag{A6}$$

Therefore,

$$z_i^+ = -\frac{p_i^+}{\kappa} + z_{i-1}^+, \tag{A7}$$

$$z_i^- = \frac{p_i^-}{\kappa} + z_{i-1}^-. \tag{A8}$$

Applying the recurrence procedure to Eqs. (A7) and (A8) we arrive to

$$z_i^+ = -\frac{1}{\kappa}\sum_{j=1}^{i} p_j^+ + z_0^+, \tag{A9}$$

$$z_i^- = \frac{1}{\kappa}\sum_{j=1}^{i} p_j^- + z_0^-. \tag{A10}$$

Taking into account that $z_0^+ = (E_0 + p_0)/\kappa = M_s/\kappa$, whereas $z_0^- = 0$ we finally get expressions for the $(t_i, z_i)$ coordinates of produced hadrons

$$z_i = \frac{1}{2\kappa}\left[M_s - \sum_{j=1}^{i}(p_j^+ + p_j^-)\right] = \frac{1}{2\kappa}\left[M_s - 2\sum_{j=1}^{i} E_j\right], \tag{A11}$$

$$t_i = \frac{1}{2\kappa}\left[M_s - \sum_{j=1}^{i}(p_j^+ - p_j^-)\right] = \frac{1}{2\kappa}\left[M_s - 2\sum_{j=1}^{i} p_j\right]. \tag{A12}$$

[1] I. Arsene *et al.* (BRAHMS Collaboration), Nucl. Phys. **A757**, 1 (2005); B. B. Back *et al.* (PHOBOS Collaboration), Nucl. Phys. **A757**, 28 (2005); J. Adams *et al.* (STAR Collaboration), Nucl. Phys. **A757**, 102 (2005); K. Adcox *et al.* (PHENIX Collaboration), Nucl. Phys. **A757**, 184 (2005).

[2] K. Aamodt *et al.* (ALICE Collaboration), Eur. Phys. J. C **68**, 89 (2010); **68**, 345 (2010); Phys. Lett. B **693**, 53 (2010).

[3] K. Khachatryan *et al.* (CMS Collaboration), J. High Energy Phys. 02 (2010) 041; K. Khachatryan *et al.* (CMS Collaboration), Phys. Rev. Lett. **105**, 022002 (2010).

[4] G. Goldhaber, S. Goldhaber, W.-Y. Lee, and A. Pais, Phys. Rev. **120**, 300 (1960).

[5] M. I. Podgoretsky, Fiz. Elem. Chastits At. Yadra **20**, 628 (1989), (in Russian).

[6] R. Lednicky, Phys. At. Nucl. **67**, 72 (2004).

[7] M. Lisa, S. Pratt, R. Soltz, and U. Wiedemann, Annu. Rev. Nucl. Part. Sci. **55**, 357 (2005).

[8] J. Adams *et al.* (STAR Collaboration), Phys. Rev. C **71**, 044906 (2005).

[9] K. Aamodt *et al.* (ALICE Collaboration), Phys. Rev. D **82**, 052001 (2010).

[10] N. S. Amelin and L. V. Bravina, Yad. Fiz. **51**, 211 (1990) [Sov. J. Nucl. Phys. **51**, 133 (1990)]; N. S. Amelin, L. V. Bravina, L. I. Sarycheva, and L. N. Smirnova, Yad. Fiz. **51**, 841 (1990) [Sov. J. Nucl. Phys. **51**, 535 (1990)].

[11] J. Bleibel, L. V. Bravina, A. B. Kaidalov, and E. E. Zabrodin, arXiv:1011.2703.

[12] A. B. Kaidalov, Phys. Lett. B **116**, 459 (1982); A. B. Kaidalov and K. A. Ter-Martirosyan, *ibid.* **117**, 247 (1982).

[13] A. Capella and J. Tran Thanh Van, Phys. Lett. B **93**, 146 (1980); A. Capella, U. Sukhatme, C.-I. Tan, and J. Tran Thanh Van, Phys. Rep. **236**, 225 (1994).

[14] V. N. Gribov, Sov. Phys. JETP **26**, 414 (1968); L. V. Gribov, E. M. Levin, and M. G. Ryskin, Phys. Rep. **100**, 1 (1983).

[15] R. D. Field and R. P. Feynman, Nucl. Phys. **B136**, 1 (1978).

[16] V. A. Abramovskii, V. N. Gribov, and O. V. Kancheli, Yad. Fiz. **18**, 595 (1973) [Sov. J. Nucl. Phys. **18**, 308 (1974)].

[17] N. S. Amelin, E. F. Staubo, and L. P. Csernai, Phys. Rev. D **46**, 4873 (1992).

[18] A. Capella, J. Tran Thanh Van, and J. Kwiecinski, Phys. Rev. Lett. **58**, 2015 (1987).

[19] J. Ranft, K. Hahn, P. Aurenche, P. Maire, F. W. Bopp, A. Capella, J. Tran Thanh Van, and J. Kwiecinski, Lawrence Berkeley Laboratory Report No. SSC-149, Berkeley, CA, 1987 (unpublished).

[20] R. Engel, J. Ranft, and S. Roesler, Phys. Rev. D **52**, 1459 (1995).

[21] S. Ostapchenko, Phys. Rev. D **83**, 014018 (2011).

[22] K. Werner, F.-M. Liu, and T. Pierog, Phys. Rev. C **74**, 044902 (2006).

[23] E. Zabrodin, C. Fuchs, L. Bravina, and Amand Faessler, Phys. Lett. B **508**, 184 (2001); E. Zabrodin, L. Bravina, C. Fuchs, and Amand Faessler, Prog. Part. Nucl. Phys. **53**, 183 (2004); G. Burau, J. Bleibel, C. Fuchs, Amand Faessler, L. V. Bravina, and E. E. Zabrodin, Phys. Rev. C **71**, 054905 (2005); J. Bleibel, G. Burau, and C. Fuchs, Phys. Lett. B **659**, 520 (2008).

[24] B. Andersson, G. Gustafson, G. Ingelman, and T. Sjostrand, Phys. Rep. **97**, 31 (1983).

[25] A. Bialas and M. Gyulassy, Nucl. Phys. **B291**, 793 (1987).

[26] M. I. Podgoretsky, Yad. Fiz. **37**, 455 (1983) [Sov. J. Nucl. Phys. **37**, 272 (1983)]; R. Lednicky, JINR Report No. B2-3-11460, 1978 (unpublished); P. Grassberger, Nucl. Phys. **B120**, 231 (1977).

[27] G. F. Bertsch, P. Danielewicz, and M. Herrmann, Phys. Rev. C **49**, 442 (1994); S. Pratt, in *Quark Gluon Plasma 2*, edited by R. C. Hwa (World Scientific, Singapore, 1995), p. 700; S. Chapman, P. Scotto, and U. Heinz, Phys. Rev. Lett. **74**, 4400 (1995).

[28] S. V. Akkelin and Yu. M. Sinyukov, Phys. Lett. B **356**, 525 (1995); Yu. M. Sinyukov, Nucl. Phys. **A566**, 589 (1994).

[29] R. Lednicky and T. Progulova, Z. Phys. C **55**, 295 (1992).

[30] G. J. Alner *et al.* (UA5 Collaboration), Phys. Rep. **154**, 247 (1987).